CrossMark

Hard X-Ray Emission from the Eastern Jet of SS 433 Powering the W50 "Manatee" Nebula: Evidence for Particle Reacceleration

Samar Safi-Harb[1] , Brydyn Mac Intyre[1], Shuo Zhang[2] , Isaac Pope[3], Shuhan Zhang[3] , Nathan Saffold[4], Kaya Mori[3] ,
Eric V. Gotthelf[3] , Felix Aharonian[5,6], Matthew Band[1,7] , Chelsea Braun[1] , Ke Fang[8] , Charles Hailey[3] ,
Melania Nynka[9] , and Chang D. Rho[10]

[1] University of Manitoba, Department of Physics & Astronomy, Winnipeg, MB R3T 2N2, Canada; samar.safi-harb@umanitoba.ca
[2] Bard College Physics Program, 30 Campus Road, Annandale-on-Hudson, NY 12504, USA
[3] Columbia Astrophysics Laboratory, 550 West 120th Street, New York, NY 10027, USA
[4] Fermi National Accelerator Laboratory, PO Box 500, Batavia, IL 60510, USA
[5] Dublin Institute for Advanced Studies, 31 Fitzwilliam Place, Dublin, Ireland
[6] Max-Planck-Institut for Nuclear Physics, P.O. Box 103980, D-69029 Heidelberg, Germany
[7] University of Manitoba, Price Faculty of Engineering, Winnipeg, MB R3T 2N2, Canada
[8] Department of Physics, Wisconsin IceCube Particle Astrophysics Center, University of Wisconsin, Madison, WI 53706, USA
[9] Kavli Institute For Astrophysics and Space Research, Massachusetts Institute of Technology, Cambridge, MA, USA
[10] University of Seoul, Seoul, Republic of Korea

Abstract

We present a broadband X-ray study of W50 (the "Manatee" nebula), the complex region powered by the microquasar SS 433, that provides a test bed for several important astrophysical processes. The W50 nebula, a Galactic PeVatron candidate, is classified as a supernova remnant but has an unusual double-lobed morphology likely associated with the jets from SS 433. Using NuSTAR, XMM-Newton, and Chandra observations of the inner eastern lobe of W50, we have detected hard nonthermal X-ray emission up to $\sim$30 keV, originating from a few-arcminute-sized knotty region ("Head") located $\lesssim$18′ (29 pc for a distance of 5.5 kpc) east of SS 433, and constrained its photon index to 1.58 ± 0.05 (0.5–30 keV band). The index gradually steepens eastward out to the radio "ear" where thermal soft X-ray emission with a temperature $kT \sim 0.2$ keV dominates. The hard X-ray knots mark the location of acceleration sites within the jet and require an equipartition magnetic field of the order of $\gtrsim$12 μG. The unusually hard spectral index from the "Head" region challenges classical particle acceleration processes and points to particle injection and reacceleration in the subrelativistic SS 433 jet, as seen in blazars and pulsar wind nebulae.

Unified Astronomy Thesaurus concepts: Supernova remnants (1667); X-ray astronomy (1810); High energy astrophysics (739); Jets (870)

1. Introduction

The W50 nebula, cataloged as a Galactic supernova remnant (SNR G39.7–2.0; Velusamy & Kundu 1974; van den Bergh 1980), is best known for its association with the microquasar SS 433, a binary system that displays precessing semirelativistic ($v = 0.26c$) jets, believed to be a stellar-mass-sized black hole analog to active galactic nuclei (AGNs; Margon 1984; Fabrika 2004). With a linear extent of $\sim$2° (east–west) × 1° (north–south), W50 is one of the largest known SNRs in our galaxy, over 200 pc × 100 pc across for the assumed distance $d_\oplus = 5.5$ kpc (Blundell & Bowler 2004). Dubbed the "Manatee" nebula for its radio appearances[11] (Elston & Baum 1987; Dubner et al. 1998; Farnes et al. 2017), the SNR's unique morphology is likely the result of its interaction with the jets from SS 433, as suggested by the location of optical filaments and the elongation of W50 aligned with the axes of the jets' precession cone. This conclusion was also reached using numerical simulations (Goodall et al. 2011). The "ears" (eastern and western radio-bright edges) of the nebula are reminiscent of the

lobes seen in active galaxies and in the bubbles associated with some ultraluminous X-ray sources. Figure 1 shows our multiwavelength image of this fascinating source.

Regions of the W50 nebula have been sampled within the field of view (FoV) of several X-ray missions: ROSAT, ASCA, and RXTE in the 1990s (Yamauchi et al. 1994; Safi-Harb & Ögelman 1997; Safi-Harb & Petre 1999) and earlier this century with XMM-Newton and Chandra (Moldowan et al. 2005; Brinkmann et al. 2007). In 2019, the Spectrum-Roentgen-Gamma (SRG)/eROSITA mission provided an unprecedented view of the whole nebula of W50/SS433 in X-rays (Khabibullin & SRG/eROSITA Consortium 2020). Overall, the X-ray emission is far from what would be expected from an evolved SNR due to (a) the morphology of the X-ray lobes filling the gap between SS 433 and the radio "ears," and within the projection of the jets' precessing cone, and (b) the X-ray spectrum softening away from SS 433, along the axes of the precessing jets. Furthermore, while the outermost region of W50, coincident with the eastern radio ear (referred to as region "e3" in Safi-Harb & Ögelman 1997), is dominated by soft thermal X-rays, for the interior (see regions "e1" to "e2" in Figure 2), hard thermal ($kT \sim 5$–12 keV) or nonthermal (photon index $\Gamma \sim 1.4$–1.6) emission is inferred (Safi-Harb & Petre 1999).

This hard spectrum implies, in the nonthermal interpretation, maximum energies of electrons of $\sim$300–450 TeV responsible for the synchrotron emission, thus unveiling a new site of
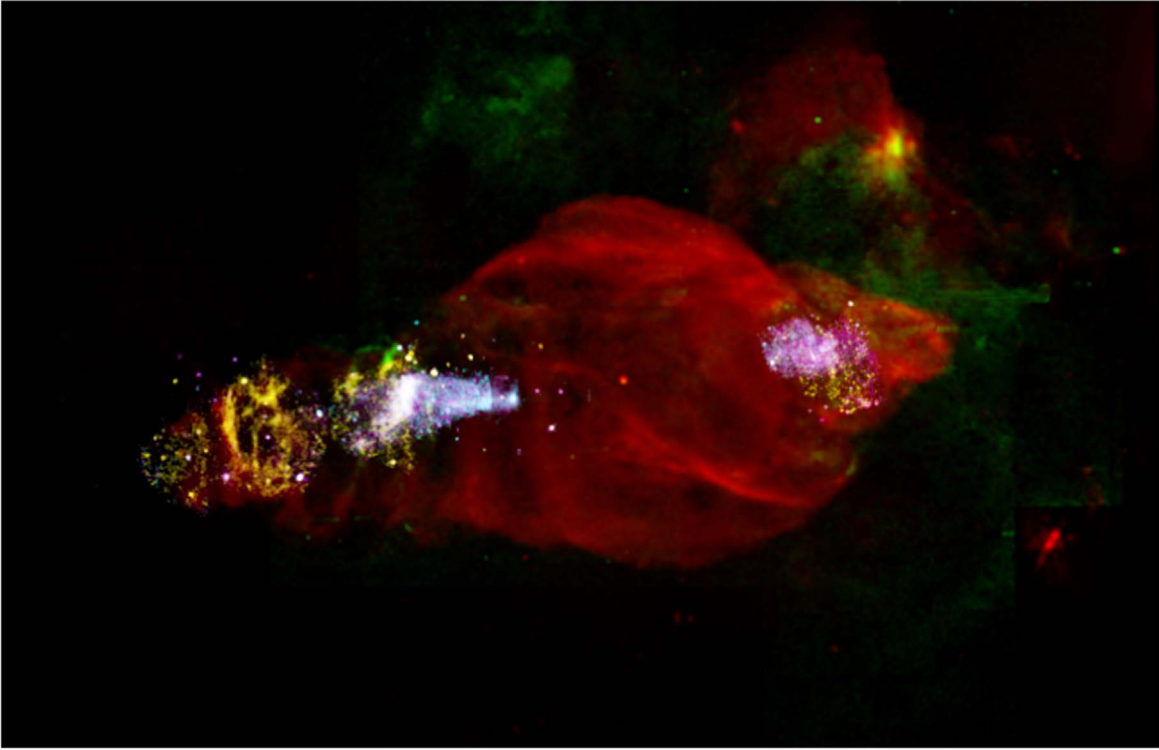

Figure 1. Multiwavelength image of the W50 nebula. Red: radio (Dubner et al. 1998); green: optical (Boumis et al. 2007); yellow: soft X-rays (0.5–1 keV); magenta: medium energy X-rays (1–2 keV); cyan: hard X-ray emission (2–12 keV). The eastern lobe X-ray image highlights the XMM-Newton data presented in this work (with the brightening at the edge of the FoV cropped here to highlight the source emission). The western lobe X-ray image shows only partial Chandra coverage of part of the nebula (Moldowan et al. 2005); additional X-ray observations of this and other regions are currently being carried out and will be presented in future work.

cosmic-ray acceleration in a jet source: a Galactic PeVatron candidate (Safi-Harb & Petre 1999; Aharonian et al. 2005). This motivated the search for high-energy, gamma-ray emission from the source using the Major Atmospheric Gamma Imaging Cherenkov telescopes (MAGIC) and the High Energy Spectroscopic System (H.E.S.S.) (MAGIC Collaboration et al. 2018), as well as the Very Energetic Radiation Imaging Telescope Array System (VERITAS; Kar & VERITAS Collaboration 2017), leading to upper limits on TeV emission from the system. The PeVatron scenario has been more recently revived with the discovery of TeV emission with the High Altitude Water Cherenkov (HAWC) Observatory (Abeysekara et al. 2018) whose peak lies close to the "e1" region. Furthermore, a recent joint Fermi-LAT and HAWC analysis (Fang et al. 2020 and references therein) finds common emission sites of GeV-to-TeV γ-rays inside the eastern and western lobes of SS 433. Despite the surge of gamma-ray studies and multiwavelength spectral energy distribution (SED) modeling of this system, the origin of the hard(est) X-ray emission, its extent/compactness, and steepness of its spectrum remain unknown.

In this paper, we present the first joint NuSTAR and XMM-Newton study of the inner eastern lobe of W50 to probe the properties of the hard X-ray emission and thus address the particle acceleration process(es) powering this Galactic PeVatron candidate. Combining new and archival XMM-Newton data and Chandra, we also present the first XMM-Newton coverage of the full eastern jet extending from SS 433 out to the radio "ear," as well as the first Chandra coverage of the innermost X-ray emitting region.

2. Observations

Three main X-ray emitting regions in the eastern lobe of W50 are defined in Safi-Harb & Ögelman (1997) and labeled "e1," "e2," and "e3," centered at 24′, 35′, and 60′ east of SS 433, respectively. For $d_{\oplus} = 5.5$ kpc, these correspond to a projected distance from SS 433 of 38 pc, 56 pc, and 96 pc, respectively. In the following, we describe new NuSTAR and XMM-Newton observations targeting region "e1" along with an archival XMM-Newton observation of "e2" and "e3" (Brinkmann et al. 2007). A Chandra observation of SS 433 (Migliari et al. 2002) serendipitously covered a portion of "e1." Summary images that outline these regions are shown in Figure 2. A list of the X-ray observations used in this study is presented in Table 1.

2.1. NuSTAR

NuSTAR observed the inner eastern lobe region, targeting region "e1," on 2019 December 1. NuSTAR consists of two coaligned X-ray telescopes coupled with focal plane detector modules FPMA and FPMB (Harrison et al. 2013). These are sensitive to X-rays in the 3−79 keV band, with a characteristic spectral resolution of 400 eV FWHM at 10 keV. The multinested foil mirrors provide 18″ FWHM (58″ HPD) imaging resolution over a 12′.2 × 12′.2 FoV. NuSTAR data were processed and analyzed using FTOOLS (HEAsoft 6.28) with NuSTAR Calibration Database (CALDB) files of 2021 January 5. The resulting data set provides a total of 109 ks, with 32 ks on a nearby off-source background field. For all subsequent analysis we merged data from the two focal plane module (FPM) detectors. Images and exposure maps were generated following the standard
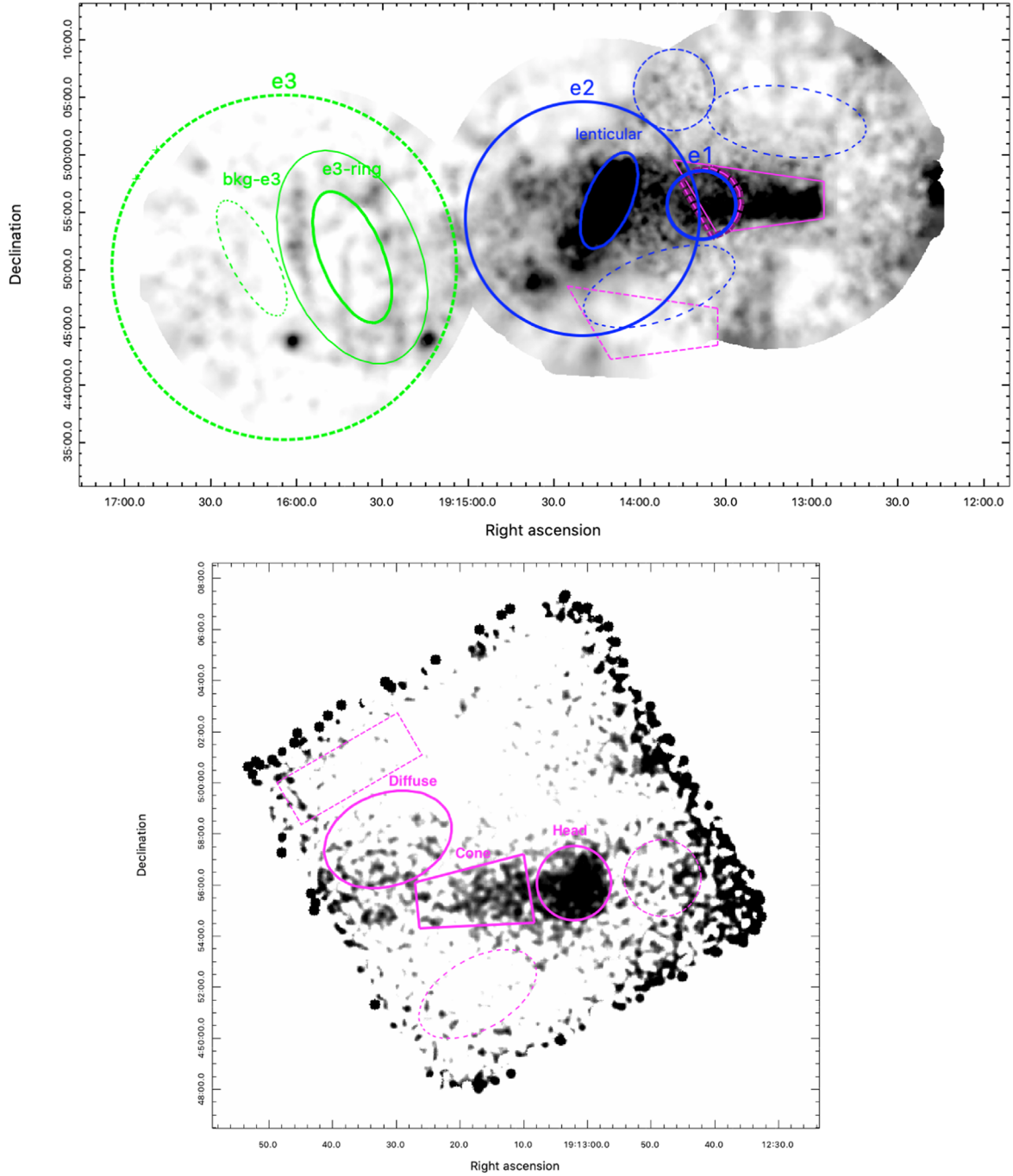
Figure 2. Top panel: XMM-Newton 0.3–10 keV mosaic image overlaid with source (solid) and background (dashed) spectral analysis regions. The "e1" and "e2" regions are shown in blue; the "e3" region (which overlaps with the radio "ear") is in green. The "lenticular" region is the brightest region within "e2." The truncated "Nue1" region in "e1" (purple dashed line) follows the edge of the NuSTAR field of view shown below. Bottom panel: the broadband 3–30 keV NuSTAR exposure-corrected and background-subtracted image showing the selected regions for the NuSTAR and joint XMM-Newton+NuSTAR spectral analysis. In both panels, the bright edges are caused by dividing by the exposure map at the edges of the FoV. The "Head," "Cone," and "Diffuse" spectral analysis regions fall within the "Full" region shown in the top panel (purple polygon).

procedure as outlined in Nynka et al. (2014), using FTOOLS extractor and `nuexpomap`. The X-ray background for the source region, which is largely dominated by stray-light photons, is estimated from the scaled off-source observation. The mirror vignetting is applied to the exposure correction.

2.2. XMM-Newton

XMM-Newton observed regions in the eastern lobe covering "e1" and part of "e2" on 2020 March 24 for 69 ks. The European Photon Imaging Camera (EPIC) on board XMM-Newton consists of three detectors, the EPIC pn detector (Strüder et al. 2001) and EPIC MOS1 and MOS2 (Turner et al. 2001). The on-axis point-spread function has an FWHM of $\sim 12''5$ and $\sim 4''3$ at 1.5 keV, for the pn and MOS, respectively. The EPIC detectors are sensitive to X-rays in the $0.15-12$ keV range with moderate energy resolution of $E/\Delta E$(pn) ~ 20–50. Data were reduced and analyzed using the Standard Analysis Software (SAS) v.19.1.0 with the most up-

Table 1
Log of the X-Ray Observations Presented in This Study

Satellite	Date	ObsID	PI	Pointing R.A., Decl. (J2000)	Total Exposure (ks)
NuSTAR	2019-12-1	40510002001	Safi-Harb, S.	19 13 11.0, +04 57 03	109,419
		40510003001		19 13 47.1, +04 46 21 (background)	32,358
XMM-Newton	2020-3-24	0840490101	Safi-Harb, S.	19 13 13.37, +04 57 29.8	69,100
XMM-Newton	2004-9-30	0075140401	Brinkmann, W.	19 14 12.01, +04 55 47.0	32,513
XMM-Newton	2004-10-4	0075140501	Brinkmann, W.	19 15 55.01, +04 51 20.0	31,314
Chandra	2000-6-27	659	Fender, R.	19 11 49.50, +04 58 58.0	9790

to-date calibration files. The source and background regions were chosen as described in detail in Section 3.2 and extracted using evselect. The response matrix file (rmf) and ancillary response file (arf) were generated for extended emission using the SAS commands rmfgen and arfgen. After filtering out background flares we obtained an effective exposure of 31/29/23 ks, for the MOS1/MOS2/pn data, respectively. We supplement our study with the archival XMM-Newton observation, carried out in 2004, covering regions "e2" to "e3." After cleaning the data, the effective exposure time is 26.7 ks for each MOS1 and MOS2 and 21.4 ks for pn.

2.3. Chandra

The innermost portion of the eastern lobe was serendipitously covered during a Chandra ACIS-S[12] observation obtained on 2000 June 27 and aimed at SS 433. We used this observation to explore the morphology and verify the spectral index of the region overlapping "e1." We reduce the data using CIAO version 4.12 (Fruscione et al. 2006) and the calibration files in the CALDB database (version 4.9.1). The event files were reprocessed from level 1 using standard procedures to remove pixel randomization and to correct for CCD charge transfer efficiencies. Response files were created using specextract, and the background was selected from a nearby source-free region south of the source and located on the same chip. The resulting effective exposure time for this observation is 9.7 ks.

3. Analysis Results

3.1. Imaging Analysis

Figure 3 (top) shows an energy resolved red–green–blue color image of the eastern lobe that combines the new and archival XMM-Newton observations. Red, green, and blue correspond to the soft (0.5–1.0 keV), medium (1.0–2.0 keV), and hard (2–10 keV) X-ray bands, respectively. The colors clearly show that (a) the innermost region of W50 is the hardest and starts at a distance closer to SS 433 than "e1"; (2) there is a mix of hard and soft X-ray emission in "e2," the brightest X-ray emitting region in the eastern lobe (lenticular, white region) where the extension of the radio shell to the north roughly intersects with the axis of the SS 433 jet (see Section 4 and Figure 8); and (3) the apparent jet–interstellar medium (ISM) termination region (coincident with the radio "ear") is dominated by soft X-ray emission with a ring-like structure (in red) that mimics the helical structure seen from the precessing SS 433 jets on much smaller scales (Migliari et al. 2002).

_____
12 https://cxc.harvard.edu/proposer/POG/html/chap6.html

Figure 3 (middle) presents the merged NuSTAR FPMA and FPMB exposure-corrected, background-subtracted image of the "e1" region in the 3–10 keV and 10–20 keV energy bands. The X-ray emission is seen to peak in the "Head" region in both the soft and hard X-ray bands, and extends into the "e1" region where the emission becomes fainter and more diffuse. In Figure 3 (bottom), we show the Chandra image with the XMM-Newton and NuSTAR contours overlaid. The "Head" emission fell on the outer S1 chip of ACIS-S and is close to its edge.

In what follows, we examine the spatial profile of the region around the "Head" to address its extent.

3.1.1. Spatial Profile with NuSTAR and XMM-Newton

In order to examine the morphology and hardness ratio throughout the eastern jet, we created linear profiles along the jet for both the soft and hard bands. The orientation and dimensions of the region used to form the linear profiles are shown in Figure 4. The profiles were primarily selected in order to study the emission around the "Head" location and were created by plotting the summed y-axis image values for each point along the x-axis.

We first sought to compare linear profiles of the jet around the "Head" region to the point spread function (PSF) of the telescope used for the observation. For the soft band, we used the XMM-Newton observation because of its superior angular resolution compared to NuSTAR. For this analysis, we only used the MOS1 image and initially binned it to $1\!.\!1$ per pixel. The profile was then binned to 10 pixels in order to smooth it without losing considerable structural information. For the background subtraction, we chose a region close to the source region and subsequently subtracted the background region profile from the source profile. The NuSTAR observation was used to create the hard band linear profile. With a pixel size of $2\!.\!46$, we chose to bin the NuSTAR profile to 6 pixels per bin. The x-axis values of the profiles were then scaled by their respective observation's pixel size in arcseconds in order to make it easier to compare the XMM-Newton and NuSTAR profiles. The NuSTAR background subtraction was done by subtracting the processed off-source image from the processed on-source image.

For comparison to the XMM MOS1 3–10 keV profile, we use the MOS1 6 keV, 3′ off-axis PSF. We compare the NuSTAR 10–20 keV profile to a NuSTAR 12–20 keV effective PSF. We normalized both the linear profiles and PSFs to unity. The XMM-Newton MOS1 and NuSTAR PSFs were then centered upon the highest value of their respective profiles. The XMM 3–10 keV profile and corresponding PSF are shown in Figure 4 (top), whereas the NuSTAR 10–20 keV and corresponding PSF are shown in Figure 4 (bottom). We note that the gaps seen in the XMM-Newton linear profile demarcate the
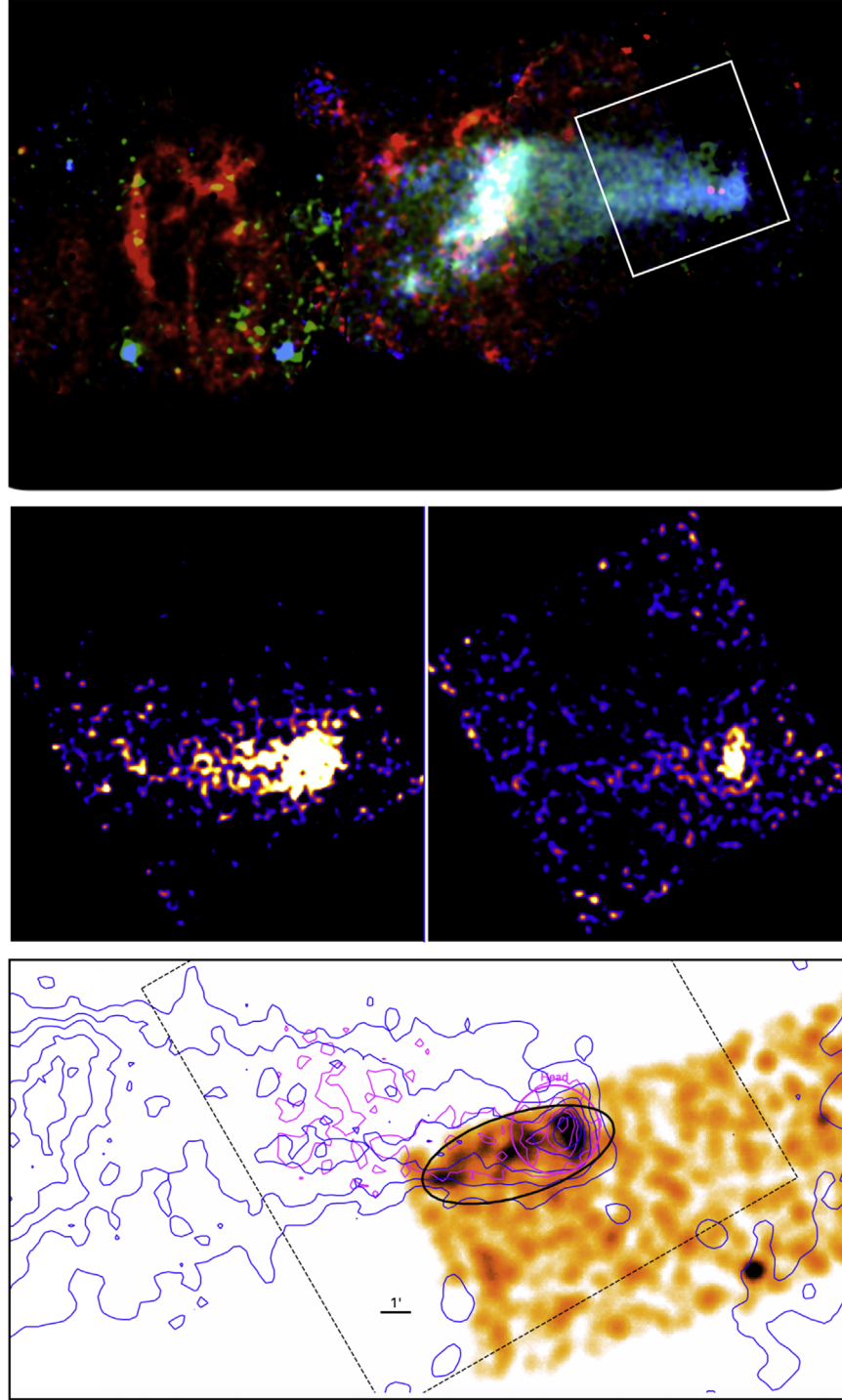
Figure 3. Top panel: an energy sliced mosaic image of W50 generated by merging exposure-corrected and smoothed new and archival XMM-Newton data. The color scheme corresponds to the 0.5–1.0 keV (red), 1.0–2.0 keV (green), and 2–10 keV (blue). The white box outlines the NuSTAR FoV shown in the next panel (containing region "e1"). Middle panel: combined NuSTAR FPMA and FPMB smoothed images in the 3–10 keV (left) and 10–20 keV (right) bands, exposure and vignetting corrected. Bottom panel: serendipitous partial Chandra coverage of the inner part of the eastern lobe. Contours are NuSTAR (magenta) and XMM-Newton (blue). The dashed box is the NuSTAR FoV, and the ellipse (black) shows the Chandra spectral extraction region that partially overlaps the "Head" region. The image is bounded by SS 433 on the right (west) and the "lenticular" region on the left (east).

MOS1 chip gap. These plots show that the "Head" region is extended compared to the nominal instrument's PSF.

In order to measure the hardness ratio along the jet, we must compare the soft and hard band linear profiles. The NuSTAR observation is however affected by ghost rays near the "Head" region. The ghost-ray contribution is more significant in the soft band, so we attempt to avoid these ghost rays by also comparing the XMM-Newton soft band profile and the NuSTAR hard band profile. We bin both the NuSTAR 3–10 keV and 10–20 keV linear profiles to 8 pixels per bin. For the XMM 3–10 keV profile, we initially bin the MOS1 image to 2″45 per pixel, close to NuSTAR's 2″46 pixel size. We then bin the XMM 3–10 keV profile to 8 pixels per bin. In order to make the XMM-Newton soft band profile comparable
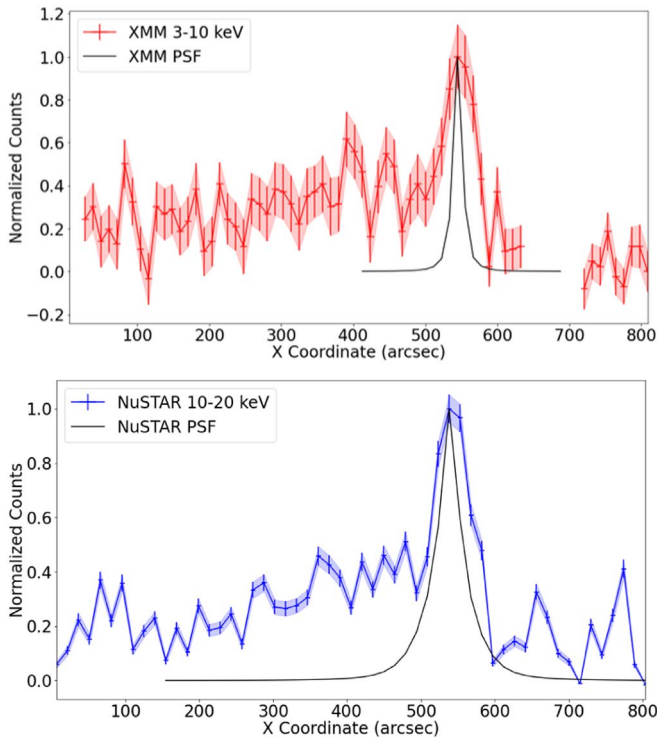
Figure 4. (Top) Background-subtracted spatial profile along the jet for the 3–10 keV XMM image compared to XMM-Newton's PSF. The XMM-Newton image used was binned to $1\rlap{.}{''}1$ per pixel in the pipeline. The XMM PSF for 6 keV and $3'$ away from on-axis position was used. Binning was set to 10 pixels. (Bottom) Background-subtracted spatial profile along the jet for the 10–20 keV NuSTAR image compared to NuSTAR's PSF. Binning was set to 6 pixels.

to the NuSTAR profiles, we scale the XMM soft band profile so that the average value of the leftmost 15 bins is normalized to the corresponding extrapolated values of the NuSTAR soft band profile. By choosing the leftmost 15 bins, we avoid the ghost rays near the "Head" region of the jet. We note that for this profile comparison, the background subtraction was done before scaling the XMM-Newton profile to the NuSTAR soft band profile. In each case, we calculate the hardness ration as H/S, where H is the number of counts from the hard band profile and S is the number of counts from the soft band profile. The various profiles and hardness ratio plots are shown in Figure 5. The NuSTAR-only and NuSTAR-XMM hardness ratio plots are similar, diverging from each other the most in the region to the right of the "Head," where we expect the greatest contribution from ghost rays. Ghost rays are further discussed in the Appendix.

3.1.2. Chandra

In order to further verify the extent of the hard X-ray emitting region and spatially resolve it, we examine the archival Chandra observation of SS 433. As illustrated in Figures 6 (inset) and 3 (bottom), this emission can be resolved into $\sim 1'$-scale knotty structures, which translate to a scale of ~ 1.6 pc at a distance $d_\oplus = 5.5$ kpc. This Chandra data set is however limited by poor statistics (see Section 3.2.2). A more detailed analysis requires a deeper and targeted Chandra observation of this region.
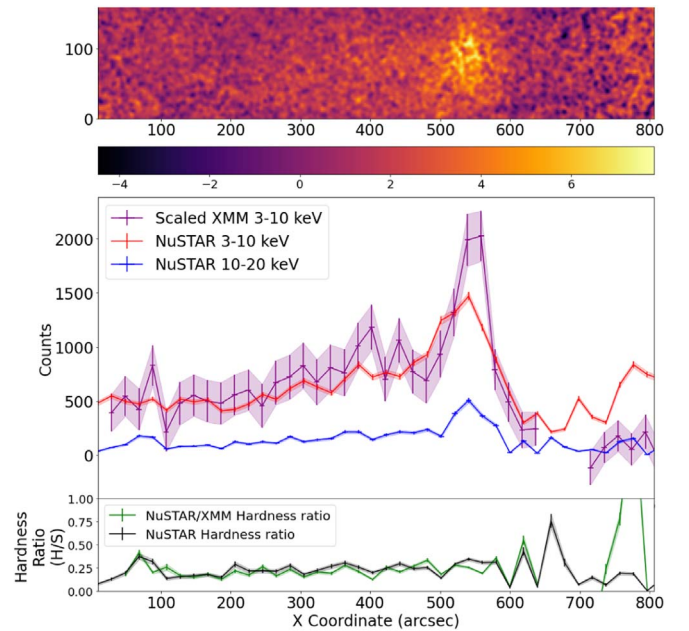

Figure 5. The scaled XMM-Newton and NuSTAR profiles around the "Head" region (top) and the hardness ratios (bottom) that diverge from each other toward SS 433 (to the right of the "Head" region), where we expect the greatest contribution from ghost rays.
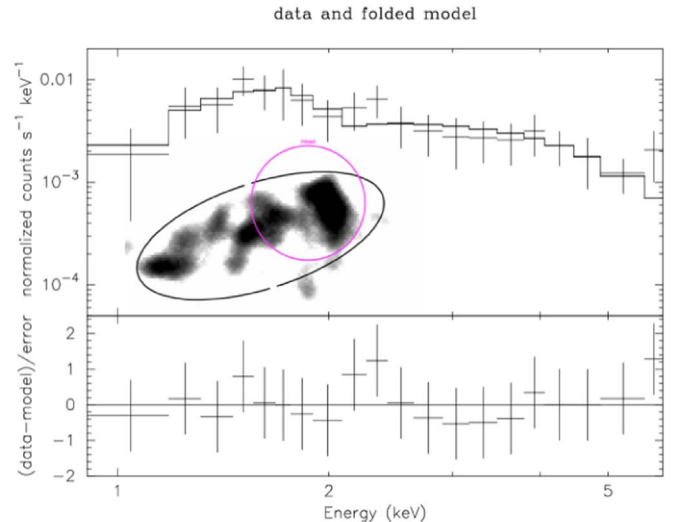

Figure 6. Chandra image (inset) and spectrum of the inner eastern lobe overlapping with the "Head" region (pink circle overlaid on the image). The image is shown on a linear scale (from 0.5 to 5 counts per pixel) and is smoothed with a Gaussian with σ of 7 pixels. The overlaid black ellipse shows the region used for extraction of the Chandra ACIS spectrum fitted with an absorbed power-law model with a photon index $\Gamma \sim 1.5$ (see Section 3.2.2).

3.2. Spectral Analysis

Guided by previous X-ray observations of the W50 system (see Section 1) we considered both nonthermal (power-law and broken power-law) models and thermal models for our spectral fits. Spectral analysis was accomplished using the X-ray spectral fitting package XSPEC v12.11.1 (Arnaud 1996)[13] with the tbabs model to describe photoelectric absorption by the interstellar medium, using the Wilms et al. (2000) abundances.

---

[13] https://heasarc.gsfc.nasa.gov/xanadu/xspec/

In general, this yields column densities, N_H, that are higher than previously published with earlier abundance models.

The XMM-Newton, NuSTAR, and Chandra data were fitted in the 0.5–10 keV, 3–30 keV, and 0.5–8.0 keV bands, respectively. The XMM-Newton spectra were grouped with a minimum of 30/50 counts per bin for MOS/pn data and 10 counts per bin for Chandra. For NuSTAR, the background-subtracted spectra are grouped for at least 3σ detection level per data bin. Since NuSTAR is not sensitive to the soft X-ray band, we fixed the column density to the value derived from XMM-Newton. The Chandra spectrum was fitted independently given its coverage of an overlapping, but not identical, region in the innermost eastern lobe (Figure 2). For all joint fits, a constant factor is used to account for calibration differences between instruments. Quoted errors are at the 90% confidence level (CL), and our fitting procedure used the chi-square (χ^2) statistic, unless otherwise noted.

3.2.1. NuSTAR and XMM-Newton Spatially Resolved Spectroscopy

Careful background subtraction is needed for the spectral analysis of the W50 lobe regions, given the nearness of W50 to the Galactic plane and its bright engine SS 433. This results in a complicated NuSTAR background due to stray light, ghost rays, and instrumental and cosmic background components. Our NuSTAR background analysis is detailed in the Appendix. For the XMM-Newton data, background selections consistent between archival and new observations were made for verification. Additionally, background selections identical to those used for the NuSTAR spectral analysis were used as an additional layer of consistency check. Over 13 background region selections, including from a nearby off-source observation, were tested before settling on the background selection shown in Figure 2. Overall, we opted for background regions that are closest to the source, source-free, and overlapping in the XMM-Newton and NuSTAR coverage given we are performing a joint spectroscopic study of the same regions selected from both telescopes.

In the following we concentrate on the hard X-ray emission from W50-east, the main focus of this work, guided primarily by the NuSTAR imaging analysis. We divided the NuSTAR spatial coverage into the three subregions shown in Figure 2, the "Head," "Cone," and "Diffuse." We also extracted a spectrum from a polygon ("Full") region to include all the above three subregions. Finally, we also examine region "Nue1," since it corresponds to the (significant) portion of the well-studied "e1" region bounded by the edge of NuSTAR's FoV and significantly overlaps with the "Diffuse" region. For each of these regions, we fitted the XMM-Newton spectra (0.5–10 keV) and the NuSTAR spectra (3–30 keV) both independently and jointly to an absorbed power-law model (const*tbabs*powerlaw in XSPEC). For the independent NuSTAR fits, we fixed the column density to the XMM-Newton value. All spectral results are presented in Table 2.

First, we find that N_H varies significantly across the inner eastern lobe, from $1.77^{+0.18}_{-0.17} \times 10^{22}$ cm^{-2} in the "Head" region, to $1.18^{+0.11}_{-0.10} \times 10^{22}$ cm^{-2} in the "Cone" region, to $0.76^{+0.11}_{-0.10} \times 10^{22}$ cm^{-2} in the "Diffuse" region. Going farther east, the column density in the "lenticular" and "e3-ring" regions are comparable to that of the "Diffuse" region (at $\sim 0.7 \times 10^{22}$ cm^{-2}). The spectral parameters shown in Table 2 correspond to the column density, N_H, frozen to its best-fit value determined from the XMM-Newton fits. We find that all

regions are adequately described by a power-law model with a photon index of 1.58 ± 0.05, 1.76 ± 0.04, and 1.77 ± 0.06 (0.5–30 keV) for the "Head," "Cone," and "Diffuse" regions, respectively. The corresponding spectra and fitted model are shown in Figure 7. When we allow N_H to vary, the error bars increase somewhat (as expected), but our results do not change (within error). These fits yield a photon index of 1.6 ± 0.1, 1.86 ± 0.08, and 1.81 ± 0.13 (0.5–30 keV) for the "Head," "Cone," and "Diffuse" regions, respectively. Taking into account the spectral results for the "lenticular" region (Table 2), we conclude that there is a gradual spectral softening eastward from SS 433 with the hardest emission at the "Head" region, the onset of X-ray emission in the eastern lobe.

The index for the "Head" region is consistent between the two instruments (at $\Gamma \sim 1.6$), whereas for the other regions, NuSTAR gave a slightly steeper index than XMM-Newton. For the larger-scale region "Full," which encompasses the source emission across the NuSTAR field, the discrepancy is primarily caused by the mixture of multiple components with different spectral indices, as demonstrated by our spatially resolved spectroscopy. For the fainter "Cone" and "Diffuse" regions, we fitted a broken power-law model to test for any steepening in the NuSTAR hard band above 10 keV. We find that this model improves on the power-law model fit for the "Cone" region, but not for the "Diffuse" nor the "Head" regions. For the "Cone," we obtain $\Gamma_1 = 1.64^{+0.04}_{-0.07}$, $\Gamma_2 = 2.1 \pm 0.1$, and a break energy $E_b = 5.3^{+0.4}_{-0.8}$ keV (F-test probability of 1.1×10^{-10}). This is likely attributed to mimicking the spectral evolution (steepening) across the wide "Cone" region extending from the "Head" toward the "lenticular" region whose index steepens to ~ 2.0.

Finally, we fitted the NuSTAR selected regions with a thermal bremsstrahlung model and measured temperatures of $kT = 18.6\ (15.6–22.7)$ keV, $10.4\ (9.4–11.4)$ keV, and $6.9\ (6.0–8.0)$ keV for the "Head," "Cone," and "Diffuse" regions, respectively. The unrealistically high temperatures, lack of emission lines, and no statistical improvement of these fits when compared to the power-law fits make us favor the power-law model over thermal models. This conclusion is in agreement with previous studies of the eastern lobe (e.g., Safi-Harb & Petre 1999 and references therein).

Further away from SS 433 toward the radio ear, the power-law photon index of the shocked bright regions (covered by XMM-Newton only) steepens to ~ 2 ("lenticular" and "e3-ring" regions), with soft thermal emission becoming evident toward these regions (see Table 2 and Figure 3). The emission becomes dominated by a thermal component with $kT \sim 0.2$ keV in the termination shock region ("e3-ring"; see also Safi-Harb & Ögelman 1997; Brinkmann et al. 2007). For this region, the total 0.5–10 keV flux is 1.2×10^{-12} erg cm^{-2} s^{-1} (observed) and 1.4×10^{-11} erg cm^{-2} s^{-1} (unabsorbed). The thermal component constitutes approximately 46% (absorbed flux of 5.6×10^{-13} erg cm^{-2} s^{-1}) and 93% (unabsorbed flux of 1.3×10^{-11} erg cm^{-2} s^{-1}) of the total flux. The properties of the thermal X-ray emission are however poorly constrained given its low surface brightness and require a deep and targeted XMM-Newton observation.

3.2.2. Chandra Spatially Resolved Spectroscopy

We extract an elliptical region (see Figure 3 and Figure 6) encompassing the "Head" region on ACIS S1 for the source and a nearby region for the background subtraction. This source significantly overlaps with the "Head" and "Cone"

Table 2
XSPEC Fits Using `const*tbabs*power` with the `cFlux` Model Added to Acquire Flux Values

	Parameter	XMM 0.5–10 keV	NuSTAR 3–30 keV	Joint 0.5–30 keV[c]
Head $N_H = 1.77 \times 10^{22}$ cm^{-2}	Photon Index Γ	1.58 ± 0.06	1.6 ± 0.1	1.58 ± 0.05
	$F[\times 10^{-12}]^{a,c}$ (abs.)	1.23 ± 0.06	2.0 ± 0.1	2.45 ± 0.07
	$F[\times 10^{-12}]^{b,c}$ (unabs.)	1.80 ± 0.06	2.0 ± 0.1	3.0 ± 0.1
	χ^2_ν (DoF)	0.96 (295)	1.19 (79)	1.00 (375)
Cone $N_H = 1.18 \times 10^{22}$ cm^{-2}	Photon Index Γ	1.65 ± 0.05	$2.00^{+0.08}_{-0.07}$	1.76 ± 0.04
	$F[\times 10^{-12}]^a$ (abs.)	1.29 ± 0.05	1.55 ± 0.09	2.13 ± 0.06
	$F[\times 10^{-12}]^b$ (unabs.)	1.81 ± 0.06	$1.58^{+0.10}_{-0.09}$	2.71 ± 0.08
	χ^2_ν (DoF)	0.96 (440)	0.98 (197)	1.03 (638)
Diffuse $N_H = 0.76 \times 10^{22}$ cm^{-2}	Photon Index Γ	1.75 ± 0.06	2.0 ± 0.2	1.77 ± 0.06
	$F[\times 10^{-12}]^a$ (abs.)	$1.02^{+0.06}_{-0.05}$	$1.00^{+0.05}_{-0.14}$	1.61 ± 0.08
	$F[\times 10^{-12}]^b$ (unabs.)	1.39 ± 0.06	$1.00^{+0.15}_{-0.14}$	1.99 ± 0.09
	χ^2_ν (DoF)	0.98 (467)	1.33 (59)	1.02 (527)
Full $N_H = 1.03 \times 10^{22}$ cm^{-2}	Photon Index Γ	1.58 ± 0.03	1.99 ± 0.07	1.65 ± 0.03
	$F[\times 10^{-12}]^a$ (abs.)	5.60 ± 0.14	8.8 ± 0.4	11.4 ± 0.2
	$F[\times 10^{-12}]^b$ (unabs.)	7.5 ± 0.2	9.0 ± 0.4	13.4 ± 0.2
	χ^2_ν (DoF)	1.03 (1589)	0.97 (98)	1.07 (1688)
Nue1 $N_H = 0.78 \times 10^{22}$ cm^{-2}	Photon Index Γ	1.73 ± 0.05	2.2 ± 0.2	1.76 ± 0.05
	$F[\times 10^{-12}]^a$ (abs.)	1.62 ± 0.07	2.0 ± 0.2	2.89 ± 0.19
	$F[\times 10^{-12}]^b$ (unabs.)	2.20 ± 0.08	2.0 ± 0.2	3.48 ± 0.12
	χ^2_ν (DoF)	1.05 (652)	1.53 (35)	1.09 (688)
Lenticular[d] $N_H = 0.71 \times 10^{22}$ cm^{-2}	Photon Index Γ	2.05 ± 0.02	⋯	⋯
	$F[\times 10^{-12}]^a$ (abs.)	3.74 ± 0.06	⋯	⋯
	$F[\times 10^{-12}]^b$ (unabs.)	5.68 ± 0.08	⋯	⋯
	χ^2_ν (DoF)	1.04 (1101)	⋯	⋯
e3-ring $N_H = 0.79 \times 10^{22}$ cm^{-2}	Photon Index Γ	$2.0^{+0.4}_{-0.5}$	⋯	⋯
	kT (keV)	0.2 ± 0.1	⋯	⋯
	χ^2_ν (DoF)	1.14 (797)	⋯	⋯

Notes. Column densities frozen to their best-fit value using the XMM-Newton data. For the "e3-ring" region, the additional component shown corresponds to a thermal (`mekal` in XSPEC) model with solar abundances. Quoted uncertainties for 90% C.L.
[a] Absorbed flux in erg cm^{-2} s^{-1}.
[b] Unabsorbed flux in erg cm^{-2} s^{-1}.
[c] For the joint 0.5–30 keV flux, we list the combined 0.5–10 keV (XMM) and 10–30 keV (NuSTAR) fluxes with the model parameters frozen to their best values from the joint fit.
[d] The larger "e2" region encompassing the "lenticular" region (see Figure 2) shows evidence of soft thermal X-ray emission with $kT \lesssim 0.2$ keV, however, with the thermal parameters poorly constrained.

regions, and its emission is dominated by that of the "Head," which was not well resolved with NuSTAR. We obtain 243 background-subtracted source counts and a spectrum best fitted with a power-law model with $N_H = 1.61^{+0.78}_{-0.62} \times 10^{22}$ cm^{-2}, $\Gamma = 1.48^{+0.50}_{-0.45}$ (1σ error range), and a flux of 5.7×10^{-13} erg cm^{-2} s^{-1} (0.5–10 keV). Freezing the column density to 1.77×10^{22} cm^{-2}, the value obtained from XMM-Newton (which is more sensitive to the soft X-ray band) for the "Head" region, we find $\Gamma = 1.57 \pm 0.39$ (90% CL), an index which is consistent with our joint spectroscopy (Section 3.2.1). We have also attempted different binning for the Chandra spectrum as well as fitting with the Cash statistic. We find a photon index that is consistent with the abovementioned value, within error. For example, binning the spectrum with a minimum of 20 counts per bin, we obtain a photon index $\Gamma = 1.6 \pm 0.4$ (90% CL) for $N_H = 1.77 \times 10^{22}$ cm^{-2}. This confirms the unusually hard photon index obtained for the "Head" region.

4. Discussion

In Figure 8, we show the multiwavelength view of W50-east. The inner, hard, X-ray lobe is sitting within a radio "hole" (or depression in radio emission), while the optical filaments partially overlap with the projection of the radio shell along the SS 433 jet axis. This multiwavelength view and spatially resolved spectroscopic study supports the picture that the "Head" represents an acceleration zone and the onset of the eastern lobe X-ray emission; the jet thermalizes first at its interaction with the SNR ("lenticular" region in "e2," which is just beyond the intersection of the extrapolated radio shell and jet axis), then at its termination shock with the ISM (radio "ear").

Our study allowed us to zoom in on a microversion of a quasar (Figures 8 and 1). In radio, W50 mimics Fanaroff–Riley II galaxies (with prominent lobes resulting from the interaction with the surroundings), but in X-rays, it mimics Fanaroff–Riley
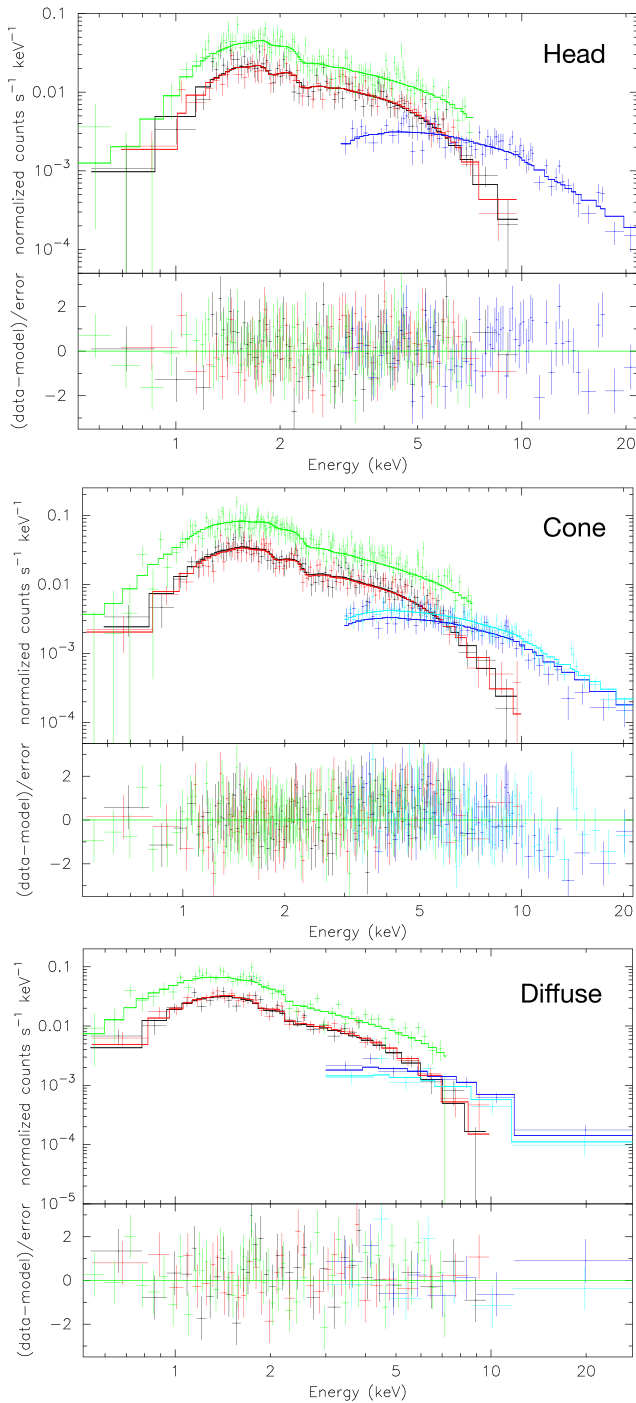
Figure 7. The joint XMM-Newton and NuSTAR spectra for the "Head" (top), "Cone" (middle), and "Diffuse" (bottom) NuSTAR regions, fitted with the absorbed power-law model as described in the text. Black, red, and green spectra correspond to MOS1, MOS2, and pn, respectively; blue and cyan correspond to the NuSTAR FPMA and FPMB spectra. The regions are shown in Figure 2, and the spectral parameters for these regions are summarized in Table 2.

I (FRI) galaxies dominated by emission from the jets close to the black hole. However, unlike FRIs, SS 433 is a super-Eddington source, accreting at a super-Eddington rate of $\sim 10^{-4}\,M_\odot\,\mathrm{yr}^{-1}$ (via Roche-lobe overflow from a massive donor star that is likely an evolved supergiant). FRIs have much lower Eddington ratios, making SS433 the nearest example of a jetted super-Eddington black hole (for a

comprehensive review, see Fabrika 2004). For W50, the jets' large-scale extended emission peaks in X-rays (as opposed to radio) given the high Lorentz factor ($\gamma \gtrsim 10^7$) of the synchrotron emitting electrons at tens of parsecs away from SS 433. Furthermore, while the nature of X-ray emission in AGN jets is being debated (synchrotron versus inverse Compton) and is more likely due to the synchrotron process in FRIs (Hardcastle et al. 2016), the nonthermal X-ray emission in W50 is most likely synchrotron emission. This is the case because, generally, synchrotron X-ray emission has been detected in microquasar jets interacting with the ISM (see, e.g., Corbel et al. 2002). Furthermore, for the estimated magnetic field in the eastern lobe (see later in this section) and hard X-ray photon index, synchrotron emission should dominate the inverse Compton flux. We add that the nonthermal bremsstrahlung process can be also ruled out since the inverse Compton flux should dominate the nonthermal bremsstrahlung flux for the electron densities inferred in the lobe (see Safi-Harb & Ögelman 1997; Safi-Harb & Petre 1999).

The SS 433/W50 system also bears resemblance to ultra-luminous X-ray sources (ULXs), a growing class of X-ray discovered compact objects believed to be associated with black holes (of debated mass) and accreting neutron stars. ULXs are bright extragalactic pointlike sources whose X-ray luminosity ($L_x \gtrsim 10^{39}\,\mathrm{erg\,s}^{-1}$) exceeds the Eddington limit for accretion into a stellar-mass black hole radiating isotropically (see Kaaret et al. 2017 for a recent review). Interestingly, SS 433 has been suggested to be the nearest Galactic ULX analog (Fabrika & Mescheryakov 2001), where its radiation can be collimated by the geometry of a funnel and beamed by the motion of the source along the line-of-sight direction (see Fabrika 2004 and references therein). However, SS 433 is aligned edge-on (or viewed from the side) with respect to Earth (Begelman et al. 2006), and its core is mostly hidden from view since it is blocked by Compton-thick material present in the plane of the accretion disk. As a result, SS 433 does not manifest itself as a typical ULX (where the disk wind would be sufficiently optically thin to allow a copious amount of X-ray photons to reach us), nor even as a luminous X-ray binary.

Bubble-like, large (~ 100–500 pc scale) shock-ionized neb-ulae have been detected, primarily in the radio and optical wavelengths, around some ULXs. Jets have been proposed to be responsible for inflating the observed bubbles (see, e.g., Pakull et al. 2010). A direct comparison with W50 would then allow us to revisit the question raised in the 1980s (Begelman et al. 1980) on whether W50 can be similarly a bubble (or "beam-bag") inflated solely by the SS 433 jets (see Section 5 in Safi-Harb & Ögelman 1997 for a discussion on the beam-bag scenario versus the favored SNR+jets scenario later verified by numerical simulations; Goodall et al. 2011). Two notable examples similar to SS 433 (in terms of the presence of powerful jets with a kinetic power exceeding $10^{39}\,\mathrm{erg\,s}^{-1}$) are NGC 7793–S26 located at a distance of ~ 3.9 Mpc (Soria et al. 2010; Pakull et al. 2010) and Holmberg II X–1 located at a distance of ~ 3.39 Mpc (Cseh et al. 2014, 2015). For S26, a 300 pc diameter jet-inflated bubble in the galaxy NGC 7793, Chandra resolved two "hot spots," in addition to the core, separated by a projected distance of $15''$ which translates to ~ 290 pc. A nonthermal (power-law or broken power-law) spectrum has been ruled out for these X-ray emitting hot spots whose spectra are best fitted by a two-component thermal plasma model ($kT_1 \sim 0.26$ keV and $kT_2 \sim 0.96$ keV). Based on
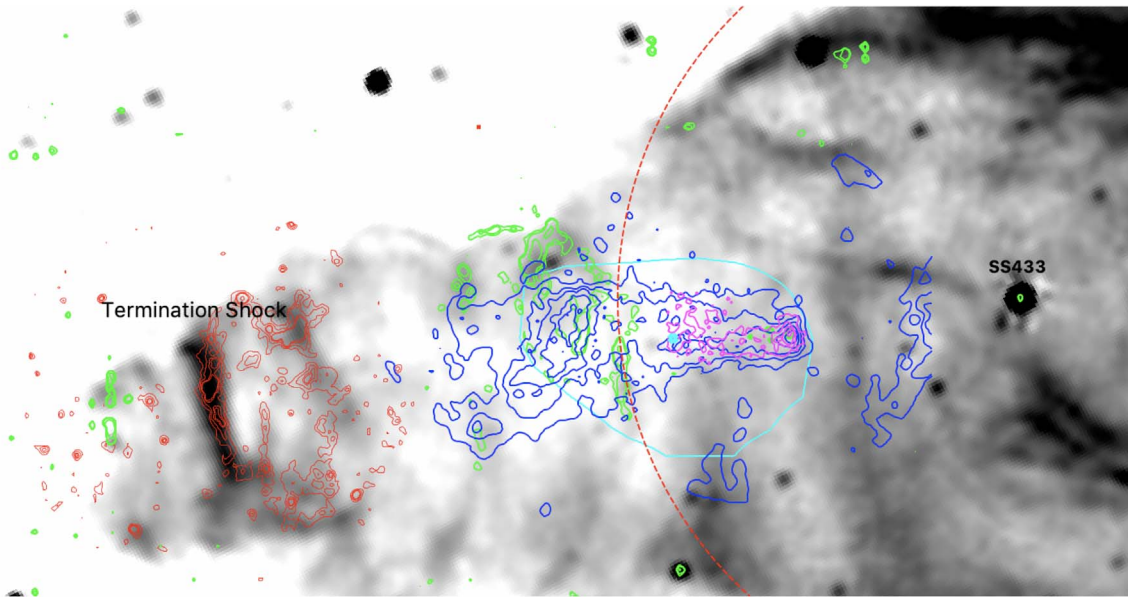
Figure 8. Multiwavelength image of the eastern lobe of W50 bounded by SS 433 to the right and the radio "ear" to the left. The radio 1.4 GHz image (Dubner et al. 1998) is shown with X-ray, optical (Boumis et al. 2007), and the HAWC emission (Abeysekara et al. 2018). Contours shown are XMM-Newton contours of the inner eastern jet covering regions "e1"–"e2" (blue), NuSTAR coverage of the innermost region jet covering "e1" (purple), XMM-Newton contours of the "e3-ring" region (red) overlapping the radio "ear" (or termination shock), optical filaments (green), and the HAWC 4σ contour (cyan). We note that the blue contour running in the north–south direction in between SS 433 and the "Head"–"e1" region delineates the edge of the XMM-Newton FoV. The dashed radio circle denotes the extent of the radio shell seen to the north and south. The inner X-ray lobe is sitting within a radio "hole" (or depression in radio emission), while the optical filaments partially overlap with the projection of the radio shell along the SS 433 jet axis.

their physical scale and X-ray spectrum, we infer that these regions could be the equivalent to the termination shock regions seen in the "ears" of W50 (region "e3" in Figure 2; see also Figure 8). The morphology (large radio cocoon and hot thermal X-ray spots) resembles W50; however, the total energy content of the W50 bubble is two orders of magnitude lower than that of S26 (Pakull et al. 2010). For Holmberg II X–1, the X-ray observations (with Swift and Chandra) show steady, apparently hard spectra; however, the X-ray emission is dominated by the emission from the core component and no extended X-ray emission or hot spots have been reported. Recent attempts to detect X-rays (using Chandra) from Holmberg IX X–1, another large (~300 pc scale, distance of 3.8 Mpc) ULX bubble, failed to detect any extended X-ray emission down to a luminosity of 2×10^{36} erg s^{-1} (Sathyaprakash et al. 2019). Finally, Chandra observations of the S10 optical nebula in NGC 300 revealed four discrete X-ray knots aligned in the plane of the sky over a length of ~150 pc (Urquhart et al. 2019). Radio observations show an elongated radio nebula (~170 pc × 55 pc in size) with its major axis aligned with the axis connecting the Chandra sources. The X-ray emission from the X-ray knots is thermal ($kT \sim 0.6$ keV), and believed to arise from the interaction between the engine (microquasar candidate) and the ISM. These properties are overall strikingly similar to W50, although (unlike W50) there is no detection of nonthermal X-ray emission in NGC 300–S10.

Based on the previously summarized observations, we conclude that while W50 shares many properties with ULX-inflated bubbles, a sensitive and detailed X-ray study of extragalactic ULX bubbles is currently hampered by their large distances, making their X-ray detection and characterization dominated by the core component (black hole) and/or the relatively bright termination shock regions on the larger scale. The latter appear to be dominated by thermal X-ray emission and are poorly resolved given the large distances (Mpc) in

comparison to Galactic distances (kpc). This again makes W50/SS 433 the most accessible ULX-bubble analog for zooming in into the outflows of these energetic sources (from close to the microquasar all the way to the termination shock) and studying their large-scale impact on their surroundings. Furthermore, while no nonthermal X-ray emission has been reported to date from the large-scale extragalactic ULX bubbles, deep and high-resolution observations in the hard ($\geqslant 2$ keV) X-ray band, with current and proposed future missions such as AXIS (Mushotzky et al. 2019) and ATHENA,[14] may reveal the equivalent of the nonthermal emission seen in W50's inner lobes on tens of parsecs scales. This emission provides clues on the jet's interaction with the ISM and the debated particle acceleration processes in play.

In this work, we have mapped the broadband X-ray emission of W50-east from SS 433 out to the radio "ear" and discovered that the hardest nonthermal X-ray emission is from the inner eastern lobe and that its peak is resolved to the "Head" region, ~18′ east of SS 433 (~29 pc at $d_\oplus = 5.5$ kpc). This emission is characterized by a hard, and rather unusual, spectral index. A photon index Γ of ~1.5 implies a particle index p of ~2 ($\frac{dN}{dE} \sim E^{-p}; p = 2\alpha + 1$ where $\alpha = \Gamma - 1$) and therefore an E^{-2} distribution of electrons. The classical diffusive shock acceleration (DSA) theory predicts a spectrum steeper than our observed X-ray spectrum. This index is in fact more similar to what is observed in pulsar wind nebulae (PWNe) powered by the relativistic winds of neutron stars (Gotthelf 2003; Kargaltsev & Pavlov 2008) and in some extragalactic jets (Harris 2003). X-ray knots in many AGN jets can also have a photon index $\Gamma \sim 1.1$–1.6 (Sambruna et al. 2004). Furthermore, such energetic electrons should be cooled; thus, to have an E^{-2}-type spectrum, one should have an extremely hard differential injection

---

spectrum, harder than E^{-1}. A possible explanation within the DSA model could be that adiabatic losses dominate over synchrotron losses as suggested for blazars to explain their hard spectra (Lefa et al. 2011). Notably, the index here steepens to an E^{-3} (for $\Gamma \sim 2$) further out as the jet thermalizes. Therefore, it is possible that particles are accelerated in the "Head" region with an E^{-2} spectrum. Inside the accelerator, the spectrum is not deformed (due to the adiabatic losses or energy-independent escape), but electrons, after they leave the source, suffer synchrotron losses that naturally can explain the steepening of the X-ray spectrum in the "Cone" and "Diffuse" regions. An alternative acceleration mechanism could be magnetic reconnection or stochastic acceleration that can produce a very hard (e.g., Maxwellian type) acceleration spectrum (Sironi & Spitkovsky 2014; Lazarian et al. 2015), which after synchrotron cooling becomes E^{-2} (independent of the acceleration spectrum). We note that the column density is highest in the "Head" region (see Section 3.2). This could be evidence of jet entrainment, which would contribute to mixing and turbulence impacting the shock acceleration process, e.g., through internal shocks (Wykes et al. 2013).

To further explore the above scenario, let us consider the synchrotron emission properties of the "Head" region, which represents the innermost region in the eastern lobe characterized by the unusually hard photon index (of 1.58). Assuming equipartition between energy in the relativistic electrons and magnetic fields, a volume of 1.58×10^{57} cm^{-3}, the observed X-ray luminosity of 1.1×10^{34} erg s^{-1} (in the 0.3–30 keV range) yields, in the synchrotron emission interpretation, an equipartition magnetic field value B of $\sim$12 μG. This estimate should be considered a lower limit since the volume could be smaller, as suggested by the clumpy structures seen in the Chandra image. The energy required to accelerate the electrons to X-ray energies in the "Head" is approximately 2.4×10^{44} erg. This yields a radiative loss timescale of the order of 1 kyr. We note that this is comparable to the synchrotron loss timescale (of $\sim$250–1400 yr) of 1–30 keV photons in a 12 μG magnetic field. Therefore, we find that the loss timescale is much smaller than the age of the system of $\lesssim$30 kyr (Safi-Harb & Ögelman 1997; Dubner et al. 1998; Goodall et al. 2011). This suggests the presence of freshly ($\lesssim$kyr timescale) injected particles in the acceleration zone.

It is commonly believed that the SS 433 jets impact the W50 nebula out to the radio ears, with a significant fraction of the jets' power going into kinetic motion or an unseen outflow. In particular, the X-ray luminosity in the eastern lobe ($L_x \sim 10^{35}$ erg s^{-1}) is a very small fraction of the SS 433 jets' power. The latter ranges from 3.2×10^{38} erg s^{-1} based on Chandra HETG data (Marshall et al. 2002) to 5×10^{39} erg s^{-1} based on XMM-Newton data (Brinkmann et al. 2005) to $\sim 10^{40}$ erg s^{-1} based on ASCA data (Kotani et al. 2006). Our study shows that the hard X-ray emission starts at $\sim$29 pc from SS 433 with a gap in X-ray emission between SS 433 and the "Head." Interestingly, compact X-ray knots were observed in the arcsecond-scale X-ray jets emitted by SS 433; their rapid variability (by a factor of 1.5–2.0 and on timescales of days to as short as hours) points to "pumping" (from SS 433) or a sequence of shocks, revealing a fast, unseen outflow in the jet (Migliari et al. 2005). This outflow from SS 433 could provide the seed particles eventually accelerated at the onset "Head" region of the eastern lobe. The jet travel time between SS 433 and the "Head" is $\sim$370 yr assuming a distance of 29 pc and a

constant velocity of 0.26 c. However, it is expected that the jet outflow has significantly decelerated by the time it has traveled that far away from SS 433. The synchrotron loss timescale of $\sim$1.5 kyr (for a 1 keV photon in a magnetic field of the order of 12 μG) is smaller than the travel time between the SS 433 jet and the "Head" if the jet's velocity is smaller than 0.065 c (19,500 km s^{-1}), a reasonable assumption. Therefore, it is likely that the hard X-ray emitting knots observed in the "Head" region are associated with the arcsecond-scale jet outflow and that the seed particles are accelerated through some nontraditional acceleration mechanism (as described above) or recently reaccelerated along the jet propagation. This phenomenon is seen in extragalactic jets (Harris 2003); at the acceleration site (where the X-rays are observed), the hard spectrum component of the synchrotron emission is expected to be visible only at the highest frequencies. This trend is also seen in PWNe where the onset of their X-ray emission corresponds to the pulsar wind termination shock (e.g., Kargaltsev & Pavlov 2008) and where a hard spectral index is observed to steepen away from the engine.

The detection of hard X-ray emission up to energies of $\sim$30 keV implies electron energies, E_e, given by $(E_e/10\text{ TeV}) \sim 0.5(B/1\text{ mG})^{-1/2}(E_\gamma/1\text{ keV})^{1/2}$ (e.g., Koyama et al. 1995). For an estimated field of 12 μG, the corresponding electron energies are $\sim$250 TeV. This supports the scenario where this unique microquasar represents an efficient site for particle acceleration up to hundreds of TeV energies. Detailed SED modeling (for leptonic versus hadronic emission models; see, e.g., Sudoh et al. 2020) and interpretation in the light of interaction between the SS 433 jet and the SNR shell will be the subject of future work that will make use of our spatially resolved X-ray spectroscopy across the eastern lobe, combined with upcoming additional TeV studies from HAWC, HESS, and hopefully LHAASO.

5. Conclusions

We presented the first joint NuSTAR and XMM-Newton observation of the eastern lobe, as well as the first Chandra snapshot of its innermost region. Our results can be summarized as follows:

1. We have detected, resolved, and characterized the hard X-ray emission from the eastern lobe of W50. The eastern jet starts at $\lesssim$18′ ($\sim$29 pc at $d_\oplus = 5.5$ kpc) from SS 433 (the "Head") and is knotty with an $\sim$1′ (1.6 pc) scale.
2. The emission from the "Head" is characterized by a hard nonthermal X-ray spectrum with a photon index $\lesssim$1.6 (confirmed with NuSTAR, XMM-Newton, and Chandra).
3. The photon index gradually steepens away from SS 433 to $\sim$1.8 in the "Cone" and "Diffuse" regions, $\sim$2 in the "lenticular" and termination shock regions, with soft thermal X-ray emission ($kT \sim 0.2$ keV) dominating the termination shock region at the radio "ear."

The hard X-ray knots mark the location of acceleration sites within the jet; the hard index challenges classical particle acceleration processes and suggests the need for an additional energizing of particles near the "Head" region. Deep and high-resolution observations of all regions in W50 (underway or planned), combined with multiwavelength SED modeling, will be the subject of future works aimed at completing our understanding of this unique system whose study is relevant to

probing the outflows of many galactic and extragalactic sources, including PWNe, AGNs, and ULXs.

Appendix
Background Analysis: NuSTAR Background Simulations

In what follows, we detail the specifics for the NuSTAR background analysis given its complex nature and potential impact on the spectral results. A diffuse X-ray source such as the eastern lobe requires analyzing the NuSTAR background contamination carefully and optimizing the background extraction regions. In general, the NuSTAR background is composed of (1) focused (2-bounce) diffuse photons, (2) ghost-ray (1-bounce) photons from bright X-ray sources located within $\sim 3'\text{--}40'$ off-axis angles, and (3) stray-light (0-bounce) photons from X-ray sources within $\sim 1°\text{--}5°$ off-axis angles (Madsen et al. 2015). The `nuskybgd` software tool is not applicable since it does not take into account additional background contamination from the Galactic Ridge X-ray emission and ghost rays from SS433. A more detailed investigation of the ghost-ray background analysis will be presented in our forthcoming paper on the western lobe where the background contamination is more severe due to its proximity to SS 433.

The off-source NuSTAR observation provides the most accurate stray-light background count rate maps since it was performed at a similar PA as the on-source observation (Mori et al. 2015). We compared the count rates from three source-free regions (b1, b2, and b3), as indicated in the NuSTAR image (Figure A1) in the FPMA and FPMB images to the corresponding regions in the off-source observation images. In the region to the west of the "Head" (b1), the count rates for both modules are higher than those extracted from the off-source observation. Our NuSTAR imaging analysis in Section 3.1 revealed the ghost-ray contamination clearly in the spatial profiles produced in different energy bands. We also found that background spectra extracted from b1 and b2 showed a hint of Fe emission lines at $E \sim 6\text{--}7\,\text{keV}$, which are not expected from the nonthermal X-ray emission in the eastern lobe. We attributed the count rate discrepancy and Fe lines to ghost-ray background photons from SS 433. In the b3 region, we found a good agreement in the count rates between the on-source and off-source observations, suggesting that it is not impacted by the ghost rays (as for b1 and b2) and that the stray-light background component is predominant.

We further investigated the level of background contamination using the off-source NuSTAR observations and NuSIM simulator. NuSIM is a Monte Carlo ray-tracing simulation tool designed for the NuSTAR mission (Zoglauer et al. 2011). While the off-source observations are used for estimating stray-light background count rates, NuSIM allows us to simulate ghost-ray events from SS 433. We simulated ghost-ray background events from SS 433 by inputting an X-ray flux of 3.7×10^{-3} photons $\text{s}^{-1}\,\text{cm}^{-2}$ (3–79 keV) which corresponds to the Swift-BAT X-ray flux averaged over ± 1 days around the NuSTAR observation of the eastern lobe. We assumed a power-law model of $\Gamma = 1.35$ as a typical X-ray spectrum of SS 433 (Marshall et al. 2002). We generated $\sim 10^5$ ghost-ray background events to reduce statistical errors and visualize their spatial distributions clearly. Then, we estimated the NuSTAR background count rates in the three source-free regions by adding the actual stray-light and simulated ghost-ray background count rates. We found that the observed and estimated background count rates in the three regions are consistent with each other within statistical errors and the Swift-BAT flux variation during the NuSTAR observation. In the b1 and b2 regions which are closer to SS 433, the ghost-ray component is more dominant accounting for $\sim 50\%$ of the total background count rates. Therefore, we extracted background spectra from b1 for the "Head" region and found consistent spectral fitting results with the XMM-Newton spectra in the 3–10 keV band (Table 2). The NuSIM simulation maps showed that the ghost-ray count rates decrease radially with the angular distance from SS 433. Beyond the b1 and b2 regions, the ghost-ray contribution is negligible as is also evident from the fact that the count rates in b3 match with those from the (stray-light dominating) off-source observations.

For the "Cone" and "Diffuse" regions where the ghost-ray background should be minimal but the stray-light background component should be most significant, we attempted background spectra from the same detector regions (as the source extraction regions) in the off-source observation, and compared the spectral fitting using local, nearby source backgrounds. We do not find any significant difference and so we opted for the local background regions (shown in Figure 2) as for the XMM-Newton region selection, especially as this background removes also any contamination from the Galactic ridge X-ray emission. Finally for the larger "Full" region, which encompasses all NuSTAR source regions, we selected an off-source background (shown as the dashed black polygon southeast of the source FoV) primarily because of the region's large size and our limited choice for a local background. We
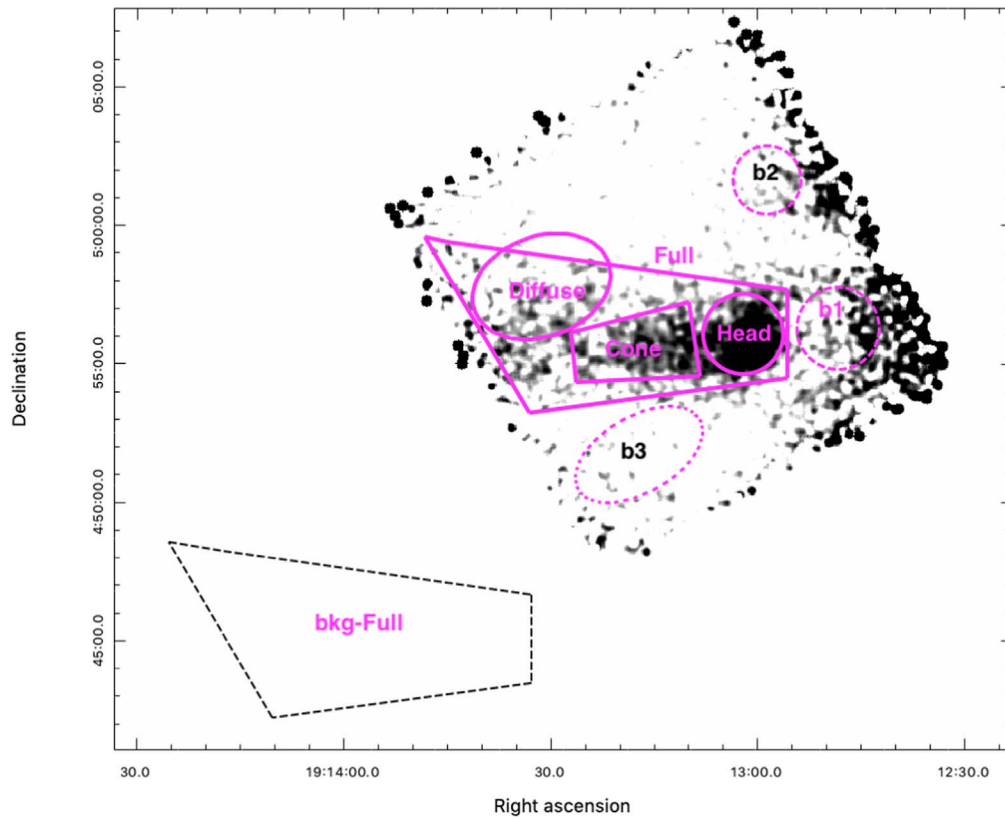
Figure A1. NuSTAR 3–10 keV image showing the background regions selected for our background analysis detailed in the Appendix text. The solid pink regions are the source regions selected for our main spectral analysis, while the dashed regions represent the background regions (b1, b2, and b3) explored for optimizing the background selection. For the "Full" source region, we chose a background from our off-source observation (dashed black polygon) with a similar PA. The final background regions selected for each of the source regions are shown in Figure 2.

believe that the apparent discrepancy between the XMM-Newton and NuSTAR spectral result for this region in particular (Table 2) is partly attributed to the impact of the NuSTAR background subtraction, but mostly because this region consists of regions characterized by different spectral components, as shown in Section 3.2.1.

ORCID iDs

Samar Safi-Harb ⓘ https://orcid.org/0000-0001-6189-7665
Shuo Zhang ⓘ https://orcid.org/0000-0002-2967-790X
Shuhan Zhang ⓘ https://orcid.org/0000-0002-0589-765X
Kaya Mori ⓘ https://orcid.org/0000-0002-9709-5389
Eric V. Gotthelf ⓘ https://orcid.org/0000-0003-3847-3957
Felix Aharonian ⓘ https://orcid.org/0000-0003-1157-3915
Matthew Band ⓘ https://orcid.org/0000-0003-2551-7586
Chelsea Braun ⓘ https://orcid.org/0000-0001-5581-486X
Ke Fang ⓘ https://orcid.org/0000-0002-5387-8138
Charles Hailey ⓘ https://orcid.org/0000-0002-3681-145X
Melania Nynka ⓘ https://orcid.org/0000-0002-3310-1946
Chang D. Rho ⓘ https://orcid.org/0000-0002-6524-9769

References

Abeysekara, A. U., Albert, A., Alfaro, R., et al. 2018, Natur, 562, 82
Aharonian, F., Akhperjanian, A., Beilicke, M., et al. 2005, A&A, 439, 635
Arnaud, K. A. 1996, in ASP Conf. Ser. 101, Astronomical Data Analysis Software and Systems V, ed. G. H. Jacoby & J. Barnes (San Francisco, CA: ASP), 17
Begelman, M. C., King, A. R., & Pringle, J. E. 2006, MNRAS, 370, 399
Begelman, M. C., Sarazin, C. L., Hatchett, S. P., McKee, C. F., & Arons, J. 1980, ApJ, 238, 722
Blundell, K. M., & Bowler, M. G. 2004, ApJL, 616, L159
Boumis, P., Meaburn, J., Alikakos, J., et al. 2007, MNRAS, 381, 308
Brinkmann, W., Kotani, T., & Kawai, N. 2005, A&A, 431, 575
Brinkmann, W., Pratt, G. W., Rohr, S., Kawai, N., & Burwitz, V. 2007, A&A, 463, 611
Corbel, S., Fender, R. P., Tzioumis, A. K., et al. 2002, Sci, 298, 196
Cseh, D., Kaaret, P., Corbel, S., et al. 2014, MNRAS, 439, L1
Cseh, D., Miller-Jones, J. C. A., Jonker, P. G., et al. 2015, MNRAS, 452, 24
Dubner, G. M., Holdaway, M., Goss, W. M., & Mirabel, I. F. 1998, AJ, 116, 1842
Elston, R., & Baum, S. 1987, AJ, 94, 1633
Fabrika, S. 2004, ASPRv, 12, 1
Fabrika, S., & Mescheryakov, A. 2001, in IAU Symp. 205, Galaxies and their Constituents at the Highest Angular Resolutions, ed. R. T. Schilizzi (San Francisco, CA: ASP), 268
Fang, K., Charles, E., & Blandford, R. D. 2020, ApJL, 889, L5
Farnes, J. S., Gaensler, B. M., Purcell, C., et al. 2017, MNRAS, 467, 4777
Fruscione, A., McDowell, J. C., Allen, G. E., et al. 2006, Proc. SPIE, 6270, 62701V
Goodall, P. T., Alouani-Bibi, F., & Blundell, K. M. 2011, MNRAS, 414, 2838
Gotthelf, E. V. 2003, ApJ, 591, 361
Hardcastle, M. J., Lenc, E., Birkinshaw, M., et al. 2016, MNRAS, 455, 3526
Harris, D. E. 2003, in ASP Conf. Ser. 300, Radio Astronomy at the Fringe, ed. J. A. Zensus, M. H. Cohen, & E. Ros (San Francisco, CA: ASP), 151
Harrison, F. A., Craig, W. W., Christensen, F. E., et al. 2013, ApJ, 770, 103
Joye, W. A., & Mandel, E. 2003, in ASP Conf. Ser. 295, Astronomical Data Analysis Software and Systems XII, ed. H. E. Payne, R. I. Jedrzejewski, & R. N. Hook (San Francisco, CA: ASP), 489
Kaaret, P., Feng, H., & Roberts, T. P. 2017, ARA&A, 55, 303
Kar, P. & VERITAS Collaboration 2017, Proc. ICRC (Busan), 35, 713
Kargaltsev, O., & Pavlov, G. G. 2008, in AIP Conf. Proc. 983, 40 Years of Pulsars: Millisecond Pulsars, Magnetars and More, ed. C. Bassa, Z. Wang, A. Cumming, & V. M. Kaspi (Melville, NY: AIP), 171

Khabibullin, I. & SRG/eROSITA Consortium 2020, The SRG/eROSITA view of the W50/SS433 (Garching: Max Planck Institute for Extraterrestrial Physics), https://events.mpe.mpg.de/event/9/contributions/339/

Kotani, T., Trushkin, S. A., Valiullin, R., et al. 2006, ApJ, 637, 486

Koyama, K., Petre, R., Gotthelf, E. V., et al. 1995, Natur, 378, 255

Lazarian, A., Eyink, G. L., Vishniac, E. T., & Kowal, G. 2015, in Magnetic Fields in Diffuse Media, ed. A. Lazarian, E. M. de Gouveia Dal Pino, & C. Melioli (Berlin: Springer), 311

Lefa, E., Rieger, F. M., & Aharonian, F. 2011, ApJ, 740, 64

Madsen, K. K., Harrison, F. A., Markwardt, C. B., et al. 2015, ApJS, 220, 8

MAGIC Collaboration, Ahnen, M. L., Ansoldi, S., et al. 2018, A&A, 612, A14

Margon, B. 1984, ARA&A, 22, 507

Marshall, H. L., Canizares, C. R., & Schulz, N. S. 2002, ApJ, 564, 941

Migliari, S., Fender, R., & Méndez, M. 2002, Sci, 297, 1673

Migliari, S., Fender, R. P., Blundell, K. M., Méndez, M., & van der Klis, M. 2005, MNRAS, 358, 860

Moldowan, A., Safi-Harb, S., Fuchs, Y., & Dubner, G. 2005, AdSpR, 35, 1062

Mori, K., Hailey, C. J., Krivonos, R., et al. 2015, ApJ, 814, 94

Mushotzky, R., Aird, J., Barger, A. J., et al. 2019, BAAS, 51, 107

Nynka, M., Hailey, C. J., Reynolds, S. P., et al. 2014, ApJ, 789, 72

Pakull, M. W., Soria, R., & Motch, C. 2010, Natur, 466, 209

Safi-Harb, S., & Ögelman, H. 1997, ApJ, 483, 868

Safi-Harb, S., & Petre, R. 1999, ApJ, 512, 784

Sambruna, R. M., Gambill, J. K., Maraschi, L., et al. 2004, ApJ, 608, 698

Sathyaprakash, R., Roberts, T. P., & Siwek, M. M. 2019, MNRAS, 488, 4614

Sironi, L., & Spitkovsky, A. 2014, ApJL, 783, L21

Soria, R., Pakull, M. W., Broderick, J. W., Corbel, S., & Motch, C. 2010, MNRAS, 409, 541

Strüder, L., Briel, U., Dennerl, K., et al. 2001, A&A, 365, L18

Sudoh, T., Inoue, Y., & Khangulyan, D. 2020, ApJ, 889, 146

Turner, M. J. L., Abbey, A., Arnaud, M., et al. 2001, A&A, 365, L27

Urquhart, R., Soria, R., Pakull, M. W., et al. 2019, MNRAS, 482, 2389

van den Bergh, S. 1980, ApJL, 236, L23

Velusamy, T., & Kundu, M. R. 1974, A&A, 32, 375

Wilms, J., Allen, A., & McCray, R. 2000, ApJ, 542, 914

Wykes, S., Croston, J. H., Hardcastle, M. J., et al. 2013, A&A, 558, A19

Yamauchi, S., Kawai, N., & Aoki, T. 1994, PASJ, 46, L109

Zoglauer, A., Kruse-Madsen, K., Kitaguchi, T., et al. 2011, AAS/High Energy Astrophysics Division, 12, 43.07